Available online at www.sciencedirect.com
ScienceDirect
Trans. Nonferrous Met. Soc. China 31(2021) 1748−1757
Transactions of Nonferrous Metals Society of China
www.tnmsc.cn

Vertical section phase diagrams of La−Fe−B ternary system

Qi WEI[1,2], Zhao LU[1,3], Qing-rong YAO[1], Jian-qiu DENG[1], Jiang WANG[1], Huai-ying ZHOU[1], Guang-hui RAO[1]

1. Guangxi Key Laboratory of Information Materials, School of Materials Science and Engineering, Guilin University of Electronic Technology, Guilin 541004, China;
2. School of Physical Science and Technology, Guangxi University, Nanning 530004, China;
3. Guangxi Key Laboratory of Processing for Non-ferrous Metals and Featured Materials, Nanning 530004, China

Received 15 June 2020; accepted 24 December 2020

Abstract: The vertical sections of the La−Fe−B system were investigated using electron probe microanalysis and differential thermal analysis. Based on the microstructures and phase compositions of the as-cast and equilibrium alloys, together with their heat flow−temperature curves, phase diagrams for three vertical sections were drawn: $La_xFe_{82}B_y$ (x+y=18), $La_xFe_{70}B_y$ (x+y=30) and $La_xFe_{53}B_y$ (x+y=47), where x and y represent mass fraction of La and B, respectively, % . Additionally, according to the phase diagrams, the compound $La_2Fe_{14}B$ was identified as a stable phase at high temperatures. It was found to be stable between 926.2 and 792.6 °C; at low temperatures, however, it decomposed into α-La, α-Fe and $LaFe_4B_4$, according to the reaction $La_2Fe_{14}B \rightarrow \alpha$-Fe+$\alpha$-La+$LaFe_4B_4$.
Key words: solidification characteristics; vertical section phase diagram; equilibrium alloy; high temperature stable compound

1 Introduction

Nd−Fe−B permanent magnet materials, which have excellent magnetic properties at room temperature, were widely used in the production of household electronic appliances, communication gadgets, medical devices and a variety of industrial products [1−5]. There has been a sharp increase in demand for Nd−Fe−B magnets, which has accelerated our excessive reliance on heavy rare earths (RE) to improve magnetic properties. This has led to the over use of key RE elements such as Nd, Pr, Dy and Tb [6−8], resulting in the current critical global RE element shortage [9]. However, there were plentiful supplies of cheap and abundant RE elements such as La and Ce [10,11]. Therefore, the development of multi-principal phase La−Ce−Nd−Fe−B permanent magnet materials will be beneficial not only to balancing the use of resources, but also to the reduction of material costs. Therefore, it has both strategic and economic significance.

Theoretically, the compound $La_2Fe_{14}B$, which has a high content of the RE element La, has good inherent permanent magnetism. Globally, it has shown promising development prospects [12]. However, it becomes unstable during sintering at high temperatures, and its magnetic performance severely deteriorates [13,14]. Generally, it is believed that the formation of a phase by this compound is relatively difficult, which affects its microstructure and magnetic properties. Recent studies have shown that permanent magnets with hard magnetic properties that fall between those of ferrites and Nd−Fe−B can still be produced from $La_2Fe_{14}B$ compound [15,16]. Therefore, an understanding of the solidification characteristics, phase transition, phase composition and thermal stability of $La_2Fe_{14}B$ in La−Fe−B system alloys is

Corresponding author: Zhao LU, E-mail: luzhao_gx@163.com; Qing-rong YAO, E-mail: qingry96@guet.edu.cn
DOI: 10.1016/S1003-6326(21)65613-3

very important regarding the development of La−Nd−Fe−B multi-phase permanent magnetic materials.

Presently, very few researchers have studied the vertical sections of RE−Fe−B ternary systems; however, the determination of their boundary binary phase diagrams has been quite successful. ENDE and JUNG [17] used thermodynamic calculations to optimize the boundary binary Fe−B system. In the Fe−B system, Fe_2B and FeB are the two insoluble intermetallic phases. Firstly, SCHLESINGER et al [18] reported that in the La−B binary system, the intermetallic compounds LaB_4 and LaB_6 are stable. Subsequently, TANG et al [19] evaluated the La−B binary phase diagram. The La−Fe binary system was investigated experimentally by MARDANI et al [20], and was thermodynamically evaluated by KONAR et al [21]. Their results showed that no intermetallic compounds were present in the system. Using differential thermal analysis, the as-cast and annealed states of $La_{76}Fe_{16}B_8$ alloys were firstly studied by HADJIPANAYIS et al [14], who found that the compound $La_2Fe_{14}B$ was an unstable phase that decomposed into Fe and an La−B alloy at low temperatures. Furthermore, an investigation of its precipitation behaviour during rapid quenching and heat treatment, conducted by ZHANG et al [22], revealed that after quenching, there was no evident hard magnetic phase (molar ratio 2:14:1); however, large quantities of Fe and La were precipitated.

Thus, to provide an important theoretical basis for the preparation of high-performance multi-main-phase (MMP) Nd−La−Ce−Fe−B magnets, here the as-cast and annealed states of three vertical section alloys in the La−Fe−B system were studied. Additionally, the precipitation and solidification processes of the $La_2Fe_{14}B$ phase were determined by observing the microstructure evolution of each alloy. Thereafter, the phase transition relationships of three vertical sections were then determined.

2 Experimental

To study the solidification characteristics, phase equilibrium transition and vertical section phase diagrams of the La−Fe−B system including 18 alloys were prepared and studied using electron probe microanalysis (EPMA) and differential scanning calorimetry (DSC). The high purity (99.99 wt.%) La, Fe and B were used as raw materials to prepare the alloy samples. In an inert atmosphere provided by high purity argon, the 18 alloys (in at.%) were prepared in an arc furnace using a non-consumable tungsten electrode. To ensure sample homogeneity, the alloys were remelted four times, and each alloy was then cut into three pieces. Two pieces were separately sealed in quartz tubes filled with high purity argon, with one annealed at 600 °C and the other annealed at 800 °C, each for 40 d. The remaining piece was polished using a diamond polishing paste (0.5 μm), and anhydrous ethanol was used as a lubricant to prevent the oxidation of the alloy surfaces during polishing. The as-cast alloys and the alloys that were quenched using ice water after annealing were then polished, and their metallographic structures were observed and analyzed using EPMA. To further determine the phase compositions of the annealed alloys, X-ray diffractometry (XRD) was used to investigate the powder of the annealed alloys. A differential scanning calorimetry (DSC) was used to determine the phase transition temperatures of the 18 alloys, so as to obtain their heat flow−temperature curves.

The solidification characteristics, phase equilibrium relations and phase transition temperatures of three vertical sections: $La_xFe_{82}B_y$ (x+y=18), $La_xFe_{70}B_y$ (x+y=30) and $La_xFe_{53}B_y$ (x+y=47), were determined by analyzing the microstructures of the as-cast and annealed alloys, as well as the heating curves obtained via DSC.

3 Results and discussion

3.1 Phase relations of as-cast alloys

To determine the solidification characteristics of the prepared alloys, the as-cast alloys were metallographically analyzed using an electron probe. Based on their primary phases and solidification paths, the as-cast alloys were divided into five categories, as shown in Table 1.

In Fig. 1(a), which shows a back-scattered electron (BSE) image of as-cast alloy Sample 6, three distinct phases can be observed: the black Fe_2B phase, the grey α-Fe phase and the white α-La phase. The figure also shows the fine binary α-Fe+α-La eutectic structure and the ternary Fe_2B+α-Fe+α-La eutectic structure. Additionally, as shown in this figure, the primary crystal phase is Fe_2B, which

Table 1 Detected primary phases and solidification paths of ternary alloys

Sample No.	Primary phase	All phases	Solidification pathway
1, 6, 17, 18	Fe_2B	Fe_2B, α-Fe, α-La	$L\rightarrow Fe_2B$; $L\rightarrow\alpha$-Fe+α-La; $L\rightarrow Fe_2B+\alpha$-Fe+$\alpha$-La
2−5, 7−10	α-Fe	Fe_2B, α-Fe, α-La	$L\rightarrow\alpha$-Fe; $L\rightarrow Fe_2B$; $L\rightarrow\alpha$-Fe+α-La; $L\rightarrow Fe_2B+\alpha$-Fe+$\alpha$-La
11	LaB_9	FeB, Fe_2B, LaB_6, LaB_9	$L\rightarrow LaB_9$; $L\rightarrow$FeB; $L\rightarrow Fe_2B+LaB_6$; $L+LaB_9\rightarrow Fe_2B+LaB_6$
12	LaB_9	Fe_2B, LaB_6, $LaFe_4B_4$, LaB_9	$L\rightarrow LaB_9$; $L\rightarrow Fe_2B$; $L\rightarrow LaFe_4B_4$; $L+LaB_9\rightarrow Fe_2B+LaB_6$
13−16	$LaFe_4B_4$	Fe_2B, $LaFe_4B_4$, α-La	$L\rightarrow LaFe_4B_4$; $L\rightarrow Fe_2B+\alpha$-La

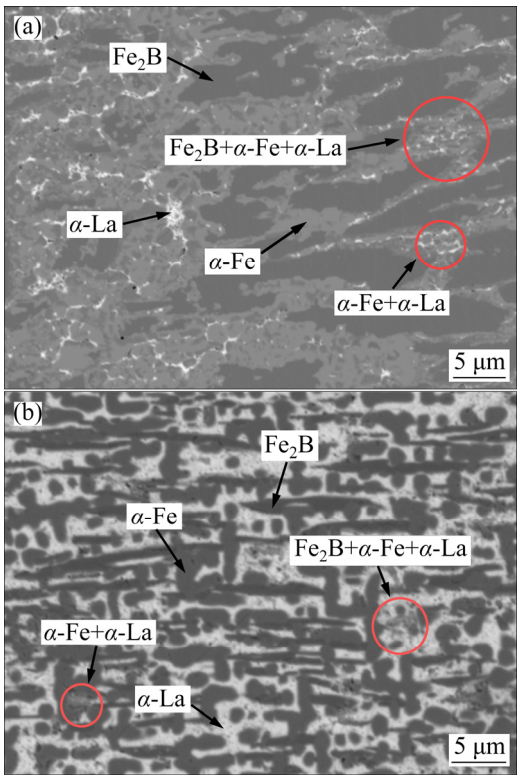

Fig. 1 BSE images of as-cast alloy Sample 6 (a) and Sample 9 (b)

is always surrounded by the single α-Fe phase. Thus, part of α-Fe is consumed during the solidification process, as a peritectic reaction occurs (thus forming Fe_2B). Moreover, a ternary eutectic structure is formed among α-Fe, α-La and the fine acicular Fe_2B phase. Based on the above analysis, the solidification sequence from the liquid phase (as the temperature decreases) can be deduced as $L\rightarrow Fe_2B$; $L\rightarrow\alpha$-Fe+α-La; $L\rightarrow Fe_2B+\alpha$-Fe+$\alpha$-La.

A BSE image of as-cast alloy Sample 9 is presented in Fig. 1(b), showing that the acicular dark, blocky light black and white phases represent Fe_2B, α-Fe and α-La, respectively. The slender, needle-like Fe_2B phase grows along the edge of the α-Fe phase. Thus, the α-Fe phase solidifies and precipitates firstly; as the temperature rapidly decreases, partial α-Fe is consumed as it reacted with B to form Fe_2B. This figure also shows that a portion of the circular α-Fe phase is surrounded by the white α-La phase, and that the melting point of the RE element, α-La, is relatively low. Thus, the α-La phase is the last to precipitate, and part of α-Fe is consumed and mutually dissolved with the α-La phase. Therefore, it can be deduced that the phase formation from the liquid phase in this alloy follows this solidification sequence: $L\rightarrow\alpha$-Fe; $L\rightarrow Fe_2B$; $L\rightarrow\alpha$-Fe+α-La; $L\rightarrow Fe_2B+\alpha$-Fe+$\alpha$-La.

A micrograph of as-cast alloy Sample 11 is shown in Fig. 2(a). Clearly, the white block represents the primary phase, LaB_9, which is the first to precipitate from the liquid phase ($L\rightarrow LaB_9$).

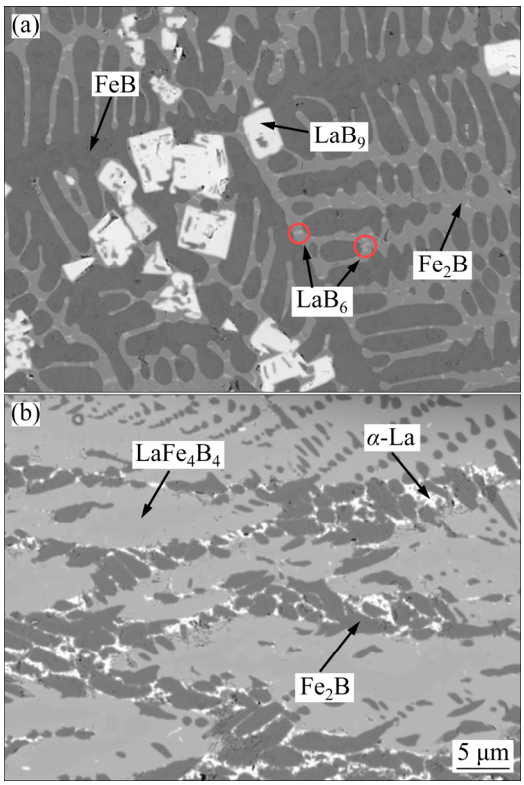

Fig. 2 BSE images of as-cast alloy Sample 11 (a) and Sample 13 (b)

The black dendrite structure represents the FeB phase (thick dendrite axis). As the solidification progresses, the FeB phase grows along the dendrite axis; thus, the primary LaB_9 crystal phase adheres to the dendrite structure of the FeB phase. Finally, the pale grey Fe_2B phase and the pale white LaB_6 phase become interwoven, and are distributed in the FeB dendrite gap. Thus, the final solidification product comprises Fe_2B and LaB_6 ($L\rightarrow Fe_2B+LaB_6$). The Fe_2B and LaB_6 phases were precipitated at the angle and gap appearing at the edge or middle of the LaB_9 phase. Evidently, the LaB_9 phase is unstable, and during solidification, it decomposes into Fe_2B and LaB_6. The solidification mode is $L+LaB_9\rightarrow Fe_2B+LaB_6$. Therefore, it can be deduced that the phase formation from the liquid phase in this alloy is in accordance with this solidification sequence: $L\rightarrow LaB_9$; $L\rightarrow FeB$; $L\rightarrow Fe_2B+LaB_6$; $L+LaB_9\rightarrow Fe_2B+LaB_6$.

A micrograph of as-cast alloy Sample 13 is shown in Fig. 2(b), in which the light grey column represents the primary $LaFe_4B_4$ crystal phase, whereas the black and white phases represent the Fe_2B and α-La phases, respectively. During the equilibrium solidification process, the B-rich phase $LaFe_4B_4$, which has the highest melting point, is the first to precipitate from the liquid phase, forming the primary crystal phase ($L\rightarrow LaFe_4B_4$). As the primary crystal phase grows, the remaining liquid phase reaches a eutectic composition, owing to the occurrence of the eutectic reaction $L\rightarrow Fe_2B+\alpha$-La. Therefore, Fe_2B and α-La grow alternately along the $LaFe_4B_4$ phase grain boundary, forming the zonal and point morphologies, respectively. The final solidified structure consists of the primary phase ($LaFe_4B_4$) and the eutectic phase ($Fe_2B+\alpha$-La).

3.2 Equilibrium phase relations

After being annealed at 600 and 800 °C for 40 d, the phase compositions of the 18 alloys were observed using EPMA, and were further determined using XRD. The experimental results are shown in Tables 2 and 3.

At 800 °C, Samples 1−5 on the $La_xFe_{82}B_y$ ($x+y=18$) vertical section consisted of two three-phase equilibrium regions (Samples 1−4, α-Fe+$Fe_2B+La_2Fe_{14}B$; Sample 5, α-Fe+β-La+ $La_2Fe_{14}B$). At 600 °C, they consisted of two three-phase equilibrium regions (Sample 1, α-Fe+$Fe_2B+LaFe_4B_4$; Samples 2−5, α-Fe+α-La+$LaFe_4B_4$). Figures 3(a) and (b) show the metallographic structures of Sample 3 at 800 and 600 °C, respectively. The phase compositions of the same alloy were different at different temperatures. Analyses of the variations in phase composition and content with temperature showed that the $La_2Fe_{14}B$ phase was stable at high temperatures, whereas at low temperatures it decomposed into α-Fe, α-La and $LaFe_4B_4$. It is worth noting that as the $LaFe_4B_4$ phase was formed by the eutectoid reaction of α-Fe+α-La+Fe_2B, the eutectic structure of α-Fe+α-La+$LaFe_4B_4$ remained after annealing, as shown in Fig. 3(b).

To determine the transition and decomposition temperatures between the phases on the vertical section of the phase diagram, the 18 samples were evaluated using a differential thermal analyser. The microstructure of the annealed samples was also analyzed. According to the heat flow−temperature curves of Samples 1−5, the $La_2Fe_{14}B$ phase was stable between 792.6 and 926.2 °C, and decomposed at 792.6 °C, as shown in Fig. 4(a) ($La_2Fe_{14}B\rightarrow\alpha$-Fe+$\alpha$-La+$LaFe_4B_4$). The blue points on the curves represent the liquid point temperatures of the five Samples, and the liquidus of the $La_xFe_{82}B_y$ vertical section ($x+y=18$) could be inferred by combining the Fe−B and La−Fe phase diagrams.

The phase relationships of Samples 6−10 on the $La_xFe_{70}B_y$ ($x+y=30$) vertical section were similar to those of the $La_xFe_{82}B_y$ ($x+y=18$) vertical section. At 600 °C, there were two three-phase equilibrium regions (Sample 6, α-Fe+$Fe_2B+LaFe_4B_4$; Samples 7−10, α-Fe+α-La+$LaFe_4B_4$). However, at 800 °C, there were three three-phase equilibrium regions (Sample 6, $Fe_2B+La_2Fe_{14}B$; Samples 7−9, β-La+$Fe_2B+La_2Fe_{14}B$; Sample 10, α-Fe+β-La+$La_2Fe_{14}B$). Given that the presence of the $La_2Fe_{14}B$ phase resulted in the formation of a new equilibrium, the tie lines of $Fe_2B-La_2Fe_{14}B$ and $La-La_2Fe_{14}B$ divided the phase regions into three three-phase equilibrium regions. Figures 3(c) and (d) show the metallographic structures of Sample 9 at 800 and 600 °C, respectively. Similarly, the phase transition temperatures and liquidus could be deduced from the heat flow−temperature curves of Samples 6−10, as shown in Fig. 4(b).

Table 2 Experimental results of La−Fe−B alloys annealed at 600 °C for 40 d

Sample No.	Composition determined using EPMA				Phase identified using XRD
	x(La)/%	*x*(Fe)/%	*x*(B)/%	Phase	
1 ($La_{2.5}Fe_{82}B_{15.5}$)	0.21	97.49	2.30	α-Fe	α-Fe, Fe_2B, $LaFe_4B_4$
	0.00	66.16	33.84	Fe_2B	
	11.35	43.68	44.97	$LaFe_4B_4$	
2 ($La_5Fe_{82}B_{13}$)	0.35	98.75	0.90	α-Fe	α-Fe, α-La, $LaFe_4B_4$
	96.49	2.51	1.00	α-La	
	10.99	42.98	46.03	$LaFe_4B_4$	
3 ($La_8Fe_{82}B_{10}$)	0.24	99.41	0.35	α-Fe	α-Fe, α-La, $LaFe_4B_4$
	2.19	97.47	0.34	α-La	
	10.32	44.83	44.85	$LaFe_4B_4$	
4 ($La_2Fe_{14}B$)	0.45	98.79	0.76	α-Fe	α-Fe, α-La, $LaFe_4B_4$
	2.00	96.59	1.41	α-La	
	11.74	44.87	43.39	$LaFe_4B_4$	
5 ($La_{15}Fe_{82}B_3$)	0.67	98.76	0.57	α-Fe	α-Fe, α-La, $LaFe_4B_4$
	98.72	0.16	1.12	α-La	
	12.03	45.39	42.58	$LaFe_4B_4$	
6 ($La_{2.5}Fe_{70}B_{27.5}$)	0.35	98.65	1.00	α-Fe	α-Fe, Fe_2B, $LaFe_4B_4$
	0.07	67.34	32.59	Fe_2B	
	11.00	42.21	46.79	$LaFe_4B_4$	
7 ($La_{10}Fe_{70}B_{20}$)	0.47	99.09	0.44	α-Fe	α-Fe, α-La, $LaFe_4B_4$
	98.50	0.24	1.26	α-La	
	11.46	44.31	44.23	$LaFe_4B_4$	
8 ($La_{15}Fe_{70}B_{15}$)	0.77	97.71	1.52	α-Fe	α-Fe, α-La, $LaFe_4B_4$
	98.69	0.17	1.14	α-La	
	11.01	42.28	46.71	$LaFe_4B_4$	
9 ($La_{20}Fe_{70}B_{10}$)	0.19	98.42	1.39	α-Fe	α-Fe, α-La, $LaFe_4B_4$
	98.21	0.14	1.65	α-La	
	11.63	44.56	43.81	$LaFe_4B_4$	
10 ($La_{27.5}Fe_{70}B_{2.5}$)	0.85	99.14	0.01	α-Fe	α-Fe, α-La, $LaFe_4B_4$
	96.97	1.58	1.45	α-La	
	10.26	42.28	47.46	$LaFe_4B_4$	
11 ($La_1Fe_{53}B_{46}$)	0.18	62.14	37.68	Fe_2B	Fe_2B, FeB, LaB_6
	0.25	51.11	48.64	FeB	
	12.40	0.42	87.18	LaB_6	
12 ($La_4Fe_{53}B_{43}$)	0.06	65.90	34.04	Fe_2B	Fe_2B, LaB_6, $LaFe_4B_4$
	12.51	0.35	87.14	LaB_6	
	11.21	43.40	45.39	$LaFe_4B_4$	
13 ($La_9Fe_{53}B_{38}$)	0.87	99.04	0.09	α-Fe	α-Fe, Fe_2B, $LaFe_4B_4$
	0.13	66.34	33.53	Fe_2B	
	11.46	43.23	45.31	$LaFe_4B_4$	
14 ($La_{11}Fe_{53}B_{36}$)	1.04	98.95	0.01	α-Fe	α-Fe, α-La, $LaFe_4B_4$
	98.16	0.53	1.31	α-La	
	11.46	43.23	45.31	$LaFe_4B_4$	
15 ($La_{20}Fe_{53}B_{27}$)	0.071	98.42	1.51	α-Fe	α-Fe, α-La, $LaFe_4B_4$
	96.31	3.411	0.28	α-La	
	11.69	43.43	44.88	$LaFe_4B_4$	
16 ($La_{30}Fe_{53}B_{17}$)	0.079	98.90	1.02	α-Fe	α-Fe, α-La, $LaFe_4B_4$
	98.85	1.14	0.01	α-La	
	11.39	42.33	46.28	$LaFe_4B_4$	
17 ($La_{36}Fe_{53}B_{11}$)	0.95	98.80	0.25	α-Fe	α-Fe, α-La, $LaFe_4B_4$
	98.60	0.30	1.10	α-La	
	11.64	42.95	45.41	$LaFe_4B_4$	
18 ($La_{46}Fe_{53}B$)	0.72	99.27	0.01	α-Fe	α-Fe, α-La, $LaFe_4B_4$
	95.02	1.92	3.06	α-La	
	11.65	43.51	44.84	$LaFe_4B_4$	

Table 3 Experimental results of La−Fe−B alloys annealed at 800 °C for 40 d

Sample No.	Composition determined using EPMA				Phase identified using XRD
	x(La)/%	*x*(Fe)/%	*x*(B)/%	Phase	
1 ($La_{2.5}Fe_{82}B_{15.5}$)	0.10	99.58	0.32	α-Fe	α-Fe, Fe_2B, $La_2Fe_{14}B$
	0.51	66.08	33.41	Fe_2B	
	11.91	81.44	6.65	$La_2Fe_{14}B$	
2 ($La_5Fe_{82}B_{13}$)	0.26	99.73	0.01	α-Fe	α-Fe, Fe_2B, $La_2Fe_{14}B$
	0.54	64.68	34.78	Fe_2B	
	12.03	82.27	5.70	$La_2Fe_{14}B$	
3 ($La_8Fe_{82}B_{10}$)	0.20	98.87	0.93	α-Fe	α-Fe, Fe_2B, $La_2Fe_{14}B$
	5.31	63.11	31.58	Fe_2B	
	12.03	82.27	5.70	$La_2Fe_{14}B$	
4 ($La_2Fe_{14}B$)	0.07	99.92	0.01	α-Fe	α-Fe, Fe_2B, $La_2Fe_{14}B$
	0.54	67.81	31.65	Fe_2B	
	12.22	81.31	6.47	$La_2Fe_{14}B$	
5 ($La_{15}Fe_{82}B_3$)	1.23	97.29	1.48	α-Fe	α-Fe, β-La, $La_2Fe_{14}B$
	97.53	1.35	1.12	β-La	
	12.47	81.32	6.21	$La_2Fe_{14}B$	
6 ($La_{2.5}Fe_{82}B_{27.5}$)	0.08	65.08	34.84	Fe_2B	Fe_2B, $La_2Fe_{14}B$
	11.95	82.31	5.74	$La_2Fe_{14}B$	
7 ($La_{10}Fe_{70}B_{20}$)	96.93	2.51	0.56	β-La	β-La, Fe_2B, $La_2Fe_{14}B$
	0.58	63.54	35.88	Fe_2B	
	12.15	81.67	6.18	$La_2Fe_{14}B$	
8 ($La_{15}Fe_{70}B_{15}$)	98.01	0.08	1.91	β-La	β-La, Fe_2B, $La_2Fe_{14}B$
	0.08	65.00	34.92	Fe_2B	
	12.34	81.46	6.20	$La_2Fe_{14}B$	
9 ($La_{20}Fe_{70}B_{10}$)	97.32	0.32	2.36	β-La	β-La, Fe_2B, $La_2Fe_{14}B$
	0.54	64.54	34.92	Fe_2B	
	12.35	82.54	5.11	$La_2Fe_{14}B$	
10 ($La_{27.5}Fe_{70}B_{2.5}$)	0.07	99.08	0.85	α-Fe	α-Fe, β-La, $La_2Fe_{14}B$
	98.37	1.37	0.26	β-La	
	11.97	81.75	6.28	$La_2Fe_{14}B$	
11 ($La_1Fe_{53}B_{46}$)	0.09	63.91	36.00	Fe_2B	Fe_2B, FeB, LaB_6
	0.10	49.60	50.30	FeB	
	14.23	0.23	85.54	LaB_6	
12 ($La_6Fe_{53}B_{41}$)	0.98	65.19	33.83	Fe_2B	Fe_2B, LaB_6, $LaFe_4B_4$
	12.56	0.12	87.32	LaB_6	
	11.98	44.20	43.82	$LaFe_4B_4$	
13 ($La_9Fe_{53}B_{38}$)	98.37	0.37	1.26	β-La	β-La, Fe_2B, $LaFe_4B_4$
	0.35	64.99	34.66	Fe_2B	
	12.22	43.86	43.92	$LaFe_4B_4$	
14 ($La_{11}Fe_{53}B_{36}$)	96.61	1.62	1.77	β-La	β-La, Fe_2B, $LaFe_4B_4$
	0.94	67.32	31.74	Fe_2B	
	11.15	43.27	45.58	$LaFe_4B_4$	
15 ($La_{20}Fe_{53}B_{27}$)	99.30	0.02	0.68	β-La	β-La, Fe_2B, $LaFe_4B_4$
	0.65	67.25	32.10	Fe_2B	
	12.06	43.62	44.32	$LaFe_4B_4$	
16 ($La_{30}Fe_{53}B_{17}$)	97.32	0.87	1.81	β-La	β-La, Fe_2B, $La_2Fe_{14}B$
	0.09	63.37	36.54	Fe_2B	
	12.19	81.17	6.64	$La_2Fe_{14}B$	
17 ($La_{36}Fe_{53}B_{11}$)	96.61	2.76	0.63	β-La	β-La, Fe_2B, $La_2Fe_{14}B$
	0.04	63.37	36.59	Fe_2B	
	12.29	81.34	6.37	$La_2Fe_{14}B$	
18 ($La_{46}Fe_{53}B$)	0.39	99.60	0.01	α-Fe	α-Fe, β-La, $La_2Fe_{14}B$
	99.02	0.64	0.34	β-La	
	12.13	82.19	5.68	$La_2Fe_{14}B$	

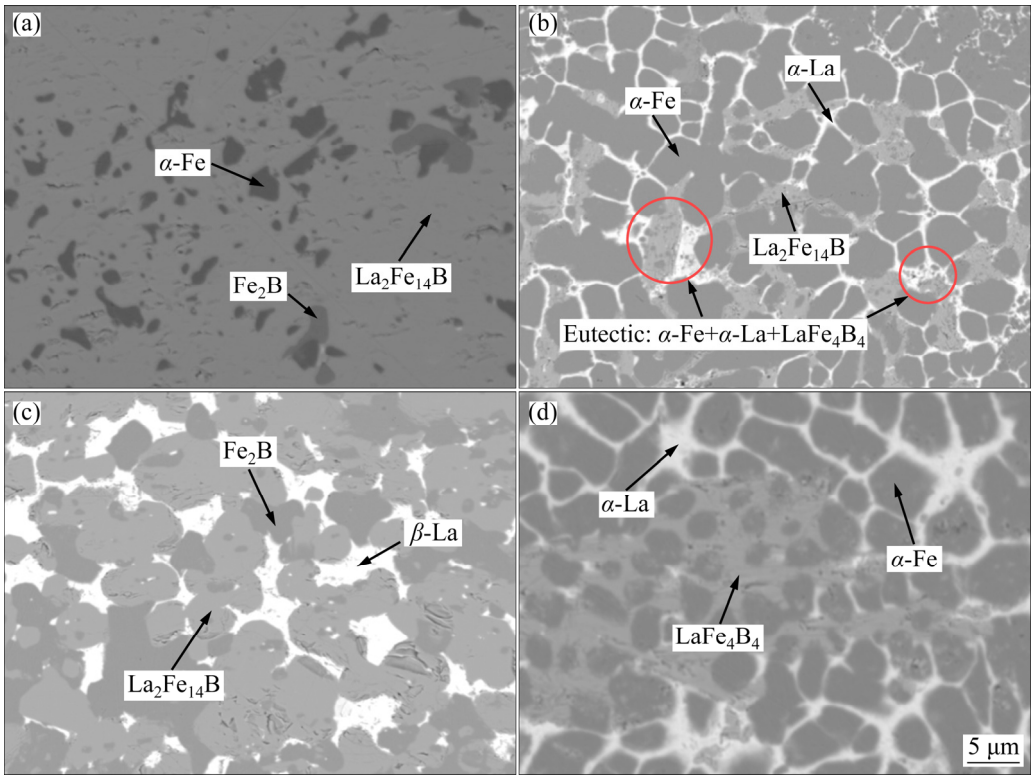

Fig. 3 BSE images of annealed Sample 3(a, b) and Sample 9(c, d) at 800 °C (a, c) and 600 °C (b, d)

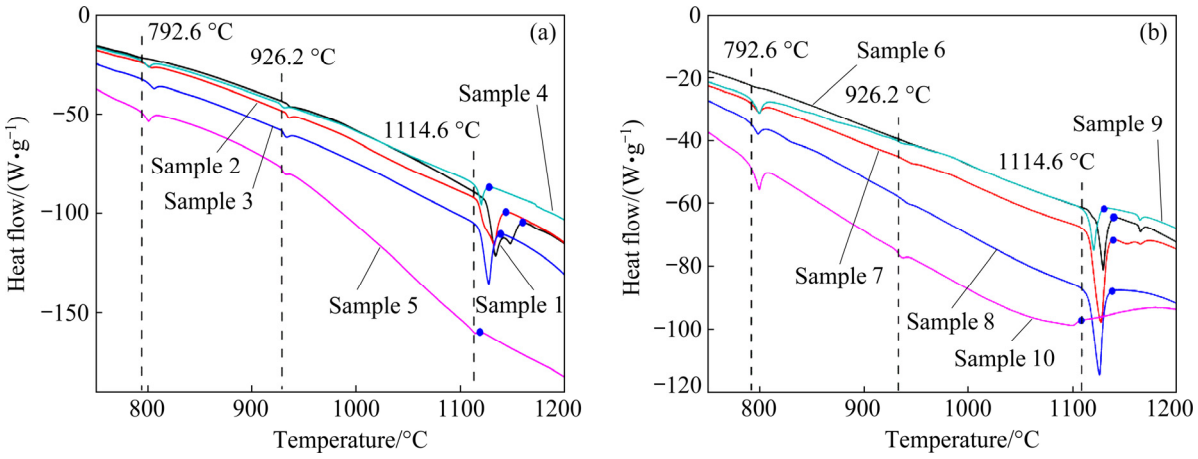

Fig. 4 DSC curves of Samples 1−5 (a) and Samples 6−10 (b)

The analysis of the microstructures of Samples 11−18 annealed at 800 and 600 °C on the $La_xFe_{53}B_y$ (x+y=47) vertical section revealed that phase equilibrium at 800 °C consisted of five three-phase equilibrium regions: Fe_2B+FeB+LaB_6, Fe_2B+LaB_6 +$LaFe_4B_4$, β-La+Fe_2B+$LaFe_4B_4$, β-La+Fe_2B+$La_2Fe_{14}B$ and α-Fe+β-La+$La_2Fe_{14}B$. The phase equilibrium at 600 °C consisted of three three-phase equilibrium regions: Fe_2B+FeB+LaB_6, Fe_2B+LaB_6+$LaFe_4B_4$ and α-Fe+α-La+$LaFe_4B_4$. Among these phases, the phase relationships of Samples 11 and 12 remained unchanged after annealing, whereas LaB_9 was completely decomposed, compared with the as-cast alloy. Due to the stable nature of the $La_2Fe_{14}B$ phase at high temperatures, the phase compositions of Samples 13−18 were different at 800 and 600 °C. According to the heat flow−temperature curves, there were $La_2Fe_{14}B$ phase transitions in Samples 16−18. Figure 5 shows the metallographic structures of Samples 11 and 13 at 800 and 600 °C. Due to the high melting point of the B-rich compound terminal, and the limited temperature rise resulting from the thermal differential analyser, the liquidus of the Fe−B

terminal could not be determined. As shown in Fig. 6, only the liquidus of the La−Fe terminal could be determined.

3.3 Phase diagrams of vertical sections

Based on the experimental results obtained after analysing the microstructures of samples in the as-cast and equilibrium states, and on the heat flow−temperature curves of the 18 samples obtained after differential thermal analysis, the solidification characteristics, phase equilibrium relationships and phase transition temperatures of three vertical sections were determined: $La_xFe_{82}B_y$ (x+y=18), $La_xFe_{70}B_y$ (x+y=30) and $La_xFe_{53}B_y$ (x+y=47). Their phase diagrams are shown in Fig. 7. The phase diagrams of the vertical sections, which were consistent with the experimental results, showed that the $La_2Fe_{14}B$ phase was stable at high temperatures, whereas at low temperatures it decomposed into the α-Fe, α-La and $LaFe_4B_4$ phases. Due to the high melting point of the $La_xFe_{53}B_y$ (x+y=47) vertical section, the Fe−B terminal compound and the limited temperature rise resulting from the equipment, the liquidus could not be determined, as shown in Fig. 7(c) (red dotted line).

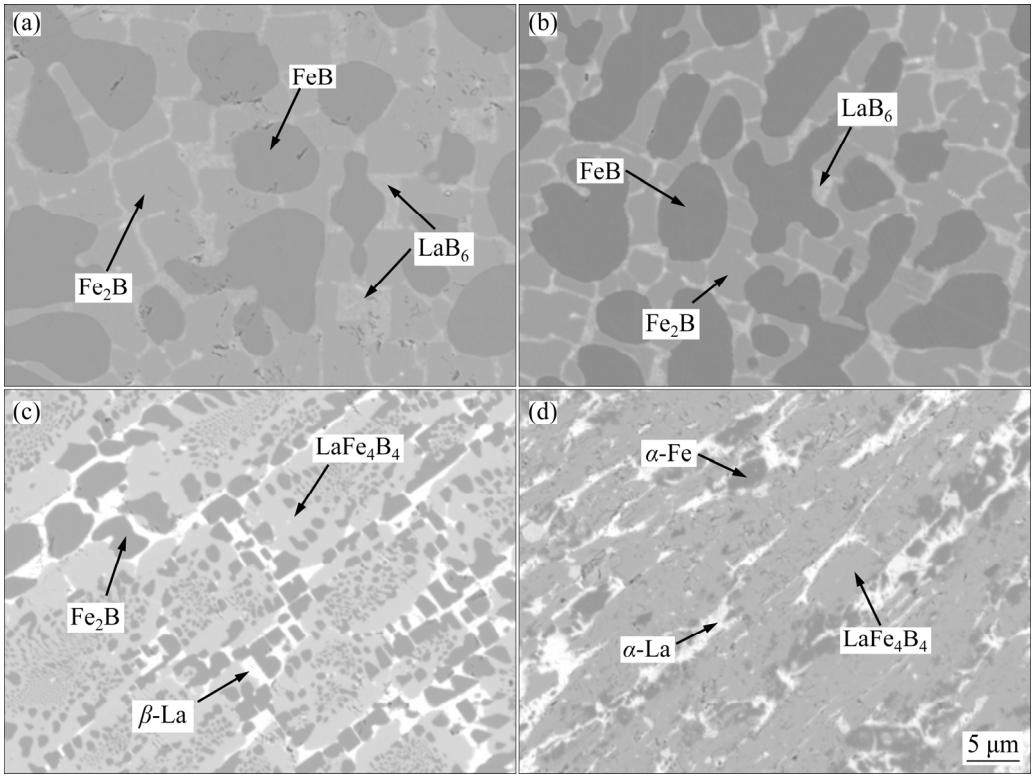

Fig. 5 BSE images of annealed Sample 11(a, b) and Sample 13(c, d) at 800 °C (a, c) and 600 °C (b, d)

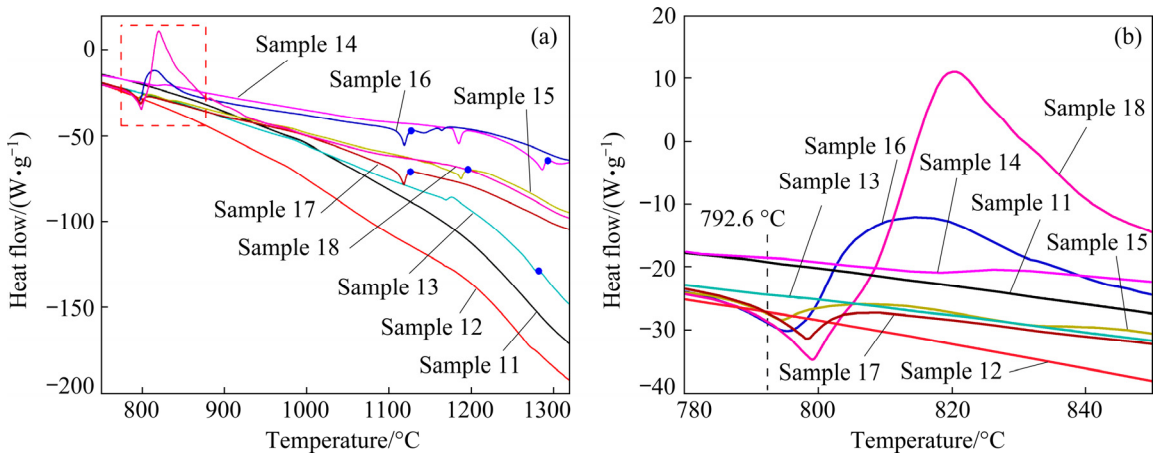

Fig. 6 DSC curves of Samples 11−18: (a) Whole temperature range; (b) Temperature range of dotted rectangle in (a)

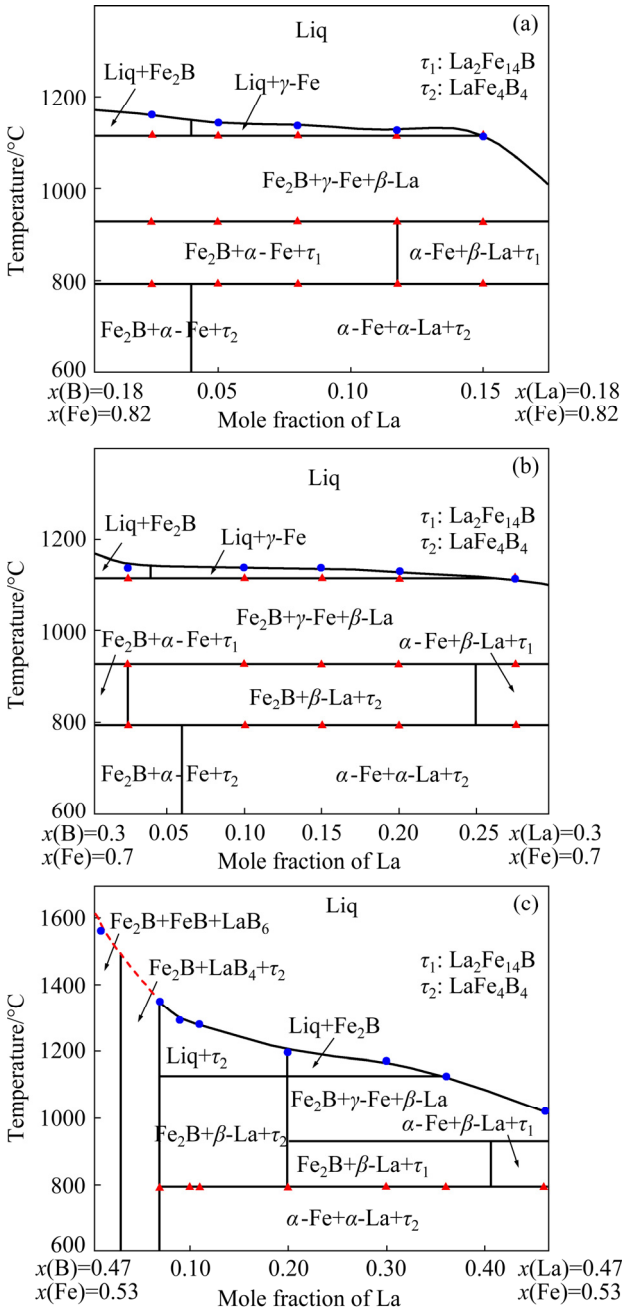

Fig. 7 Phase diagrams of three vertical sections of La−Fe−B ternary system: (a) $La_xFe_{82}B_y$ (x+y=18); (b) $La_xFe_{70}B_y$ (x+y=30); (c) $La_xFe_{53}B_y$ (x+y=47)

4 Conclusions

(1) The phase diagrams of three vertical sections of the La−Fe−B system ($La_xFe_{82}B_y$ (x+y=18), $La_xFe_{70}B_y$ (x+y=30) and $La_xFe_{53}B_y$ (x+y=47)) were drawn by analyzing 18 samples, both as-cast and after annealing, as well as their DSC curves.

(2) Based on the phase diagrams of the vertical sections and the heat flow−temperature curves of the alloys, $La_2Fe_{14}B$ was found to be stable at high temperatures between 792.6 and 926.2 °C, whereas at low temperatures it decomposed into the α-Fe, α-La and $LaFe_4B_4$ phases ($La_2Fe_{14}B \rightarrow \alpha$-Fe+$\alpha$-La+$LaFe_4B_4$).

(3) The solidification characteristics and phase transition relationships of the Fe-rich terminal in the La−Fe−B system can be successfully analyzed experimentally, providing a theoretical basis for the research and development of MMP permanent magnetic materials.

Acknowledgments

This work was financially supported by the Natural Science Foundation of China (No. 51761007), the Guangxi Natural Science Foundation, China (Nos. 2019GXNSFAA245003, 2018GXNSFAA294069, 2020GXNSFFA297004, 2021GXNSFDA075009), the Guangxi Project of Science and Technology, China (Nos. AD19110078, AA18242023-1), the Scientific Research Foundation of Guilin University of Electronic Technology, China (No. UF18016), the Guangxi Key Laboratory of Processing for Non-ferrous Metals and Featured Materials (No. 2019-GXYSOF08), China, the Guangxi Key Laboratory of Information Materials, China (No. 191012-Z), and the National Key R&D Program of China (No. 2016YFB0700901). The authors thank the financial support from the foundation for Guangxi Bagui scholars, China.

References

[1] YAO Q R, SHEN Y H, YANG P C, ZHOU H Y, RAO G H, DENG J Q, WANG Z M, ZHONG Y. Crystal structure and phase relations of $Pr_2Fe_{14}B$−$La_2Fe_{14}B$ system [J]. Journal of Rare Earths, 2016, 34: 1121−1125.

[2] YAO Q R, XIONG J L, LIU P, ZHOU H Y, RAO G H, DENG J Q, PAN S K, WANG J. Determination of the phase diagrams of the $Nd_2Fe_{14}B$−$Pr_2Fe_{14}B$ isopleth [J]. Journal of Alloys and Compounds, 2015, 633: 229−232.

[3] SEPEHRI A H, OHKUBO T, HONO K. The mechanism of coercivity enhancement by the grain boundary diffusion process of Nd−Fe−B sintered magnets [J]. Acta Materialia, 2013, 61: 1982−1990.

[4] ZHOU H Y, LAN X X, WANG Z M, YAO Q R, NI C Y, LIU W P. Effect of rapid solidification on phase structure and hydrogen storage properties of $Mg_{70}(Ni_{0.75}La_{0.25})_{30}$ alloy [J]. International Journal of Hydrogen Energy, 2012, 37: 13178−13184.

[5] LI X Q, LI L, HU K, CHEN Z C, QU S G, YANG C.

Microstructure and magnetic properties of anisotropic Nd−Fe−B magnetsprepared by spark plasma sintering and hot deformation [J]. Transactions of Nonferrous Metals Society of China, 2014, 24: 3142−3151.

[6] LIAO X F, ZHANG J S, YU H Y, ZHONG X C, ZHAO L Z, XU K, PENG D R, LIU Z W. Maximizing the hard magnetic properties of melt-spun Ce−La−Fe−B alloys [J]. Journal of Materials Science, 2019, 54: 7288−7299.

[7] XU K S, LI H W, LUO Y, WANG L, YU D B, WANG L G, YU D B, WANG Z L, PENG H J, ZHANG Y H. Experimental and computational study on the phase formation and magnetic properties of Ce−La−Fe−B alloys [J]. Journal of Magnetism and Magnetic Materials, 2018, 461: 100−105.

[8] JIN J, WANG Z, BAI G, PENG B, LIU Y, YAN M. Microstructure and magnetic properties of core-shell Nd−La−Fe−B sintered magnets [J]. Journal of Alloys and Compounds, 2018, 749: 580−585.

[9] GUTFLESISCH O, WILLARD M A, BRUCK E, CHEN C H, SANKAR S G, LIU J P. Magnetic materials and devices for the 21st century: Stronger, lighter, and more energy efficient [J]. Advanced materials, 2011, 23: 821−842.

[10] KOEN B, PETER T J, TORSTEN M, LOURDES Y. Rare earths and the balance problem: How to deal with changing? [J]. Journal of Sustainable Metallurgy, 2018, 4: 126−146.

[11] ZHANG M, LI Z B, SHEN B G, HU F X, SUN J R. Permanent magnetic properties of rapidly quenched $(La,Ce)_2Fe_{14}B$ nanomaterials based on La−Ce mischmetal [J]. Journal of Alloys and Compounds, 2015, 651: 144−148.

[12] TANG W Z, ZHOU S Z, WANG R. Preparation and microstructure of La-containing R−Fe−B permanent magnets [J]. Journal of Applied Physics, 1989, 65: 3142−3145.

[13] LIU X B, ALTOUNIAN Z, HUANG M, ZHANG Q, LIU J P. The partitioning of La and Y in Nd−Fe−B magnets: A first-principles study [J]. Journal of Alloys and Compounds, 2013, 549: 366−369.

[14] HADJIPANAYIS G C, TAO Y F, GUDIMETTA K. Formation of $Fe_{14}La_2B$ phase in as-cast and melt-spun samples [J]. Applied Physics Letters, 1985, 47: 757−758.

[15] LAI R S, CHEN R J, YIN W Z, TANG X, WANG Z X, JIN C X, LEE D, YAN A. High performance (La, Ce, Pr, Nd)−Fe−B die-upset magnets based on misch-metal [J]. Journal of Alloys and Compounds, 2017, 724: 275−279.

[16] LI Z B, SHEN B G, ZHANG M, HU F X, SUN J R. Substitution of Ce for Nd in preparing $R_2Fe_{14}B$ nanocrystalline magnets [J]. Journal of Alloys and Compounds, 2015, 628: 325−328.

[17] van ENDE M A, JUNG I H. Critical thermodynamic evaluation and optimization of the Fe−B, Fe−Nd, B−Nd and Nd−Fe−B systems [J]. Journal of Alloys and Compounds, 2013, 548: 133−154.

[18] SCHLESINGER M E, LIAO P K, SPEAR K E. The B−La (boron−lanthanum) system. Phase diagram evaluations: Section II [J]. Journal of Phase Equilibria and Diffusion, 1999, 20: 73−78.

[19] TANG Y, HU B, WANG J, GAO Q N, DU Y, YUAN X M, ZIVKOVIC D. Thermodynamic modeling of the La−B and La−Bi systems supported by first-principles calculations [J]. Journal of Phase Equilibria and Diffusion, 2013, 34: 297−306.

[20] MARDANI M, FARTUSHNA I, KHVAN A, CHEVERIKIN V, DINSDALE A. Experimental investigation of phase transformations in the La−Fe and La−Fe−C systems [J]. Calphad, 2019, 65: 370−384.

[21] KONAR B, KIM J, JUNG I H. Critical systematic evaluation and thermodynamic optimization of the Fe−RE system: RE=La, Ce, Pr, Nd and Sm [J]. Journal of Phase Equilibria and Diffusion, 2016, 37: 438−458.

[22] ZHANG Z Y, ZHAO L Z, ZHANG J S, ZHONG X C, QIU W Q, JIAO D L, LIU Z W. Phase precipitation behavior of rapidly quenched ternary La−Fe−B alloy and the effects of Nd substitution [J]. Materials Research Express, 2017, 4: 1−7.

La−Fe−B 三元合金体系的垂直截面相图

韦 奇[1,2]，卢 照[1,3]，姚青荣[1]，邓建秋[1]，王 江[1]，周怀营[1]，饶光辉[1]

1. 桂林电子科技大学 材料科学与工程学院 广西信息材料重点实验室，桂林 541004；
2. 广西大学 物理科学与工程技术学院，南宁 530004；
3. 广西有色金属及特色材料加工重点实验室，南宁 530004

摘 要：采用电子探针显微分析和差热分析研究 La−Fe−B 体系的垂直截面。根据铸态合金和平衡合金的显微组织和相组成及其热流−温度曲线，绘制 3 个垂直截面相图：$La_xFe_{82}B_y$($x+y$=18)、$La_xFe_{70}B_y$($x+y$=30)和 $La_xFe_{53}B_y$($x+y$=47)(x 和 y 分别为 La 和 B 的质量分数，%)。此外，根据相图，化合物 $La_2Fe_{14}B$ 被确定为高温稳定相。该化合物在 926.2~792.6 °C 范围内稳定存在，低温下分解为 α-La、α-Fe 和 $LaFe_4B_4$，其反应方式为 $La_2Fe_{14}B \rightarrow \alpha\text{-Fe}+\alpha\text{-La}+LaFe_4B_4$。

关键词：凝固特征；垂直截面相图；平衡合金；高温稳定化合物

(Edited by Wei-ping CHEN)